

X-Ray and Infrared Observations of Embedded Young Stars in L1630

Theodore Simon¹, Sean M. Andrews¹ and John T. Rayner¹

*Institute for Astronomy, University of Hawaii
2680 Woodlawn Drive, Honolulu, HI 96822*

Stephen A. Drake

HEASARC, NASA/GSFC, Greenbelt, MD 20771

ABSTRACT

The HH 24–26 star forming region within the Lynds 1630 (L1630) dark cloud in Orion contains a remarkable collection of rare Class 0 and Class I protostars, collimated molecular and ionized jets, and a luminous but spatially unresolved ASCA X-ray source. To study the X-ray properties of the embedded protostar population of that region, we have obtained a deep X-ray image with the ACIS-S camera on board the *Chandra X-Ray Observatory*. A number of H α emission-line objects were detected in the areas surrounding HH 24–26, of which the weak-line T Tauri star SSV 61 was the brightest source, at a steady luminosity of $L_x(0.3\text{--}10 \text{ keV}) = 10^{31.9} \text{ ergs s}^{-1}$. Two Class I protostars aligned with optical jets in HH 24, SSV 63E and SSV 63W, were also detected, as was the continuum radio source SSV 63NE, which is very likely an extreme Class I or Class 0 object. We observed no X rays from the Class 0 protostars HH 24-MMS and HH 25-MMS, nor any from regions of the cloud bounded by HH 25 and HH 26, at a 2σ upper limit of $L_x \sim 10^{30.0} \text{ ergs s}^{-1}$. HH 26-IR, the Class I object thought to be the origin of the HH 26 flow, was not detected. Near-infrared spectroscopy obtained at the NASA IRTF reveals 3 μm ice bands in the spectra of SSV 59, 63E, 63W, and HH 26-IR, and 2.3 μm CO overtone absorption bands for SSV 61. SSV 60, which lies astride one end of the great arc of nebulosity forming HH 25, exhibits a deep infrared ice band and CO absorption, but is not an X-ray source, and is most likely a distant background giant of late spectral type.

Subject headings: infrared: stars — ISM: Herbig–Haro objects — ISM: individual (L1630, HH 24–26) — stars: individual (SSV 61, SSV 63) — stars: pre-main sequence — X-rays: stars

¹Visiting Astronomer at the Infrared Telescope Facility, which is operated by the University of Hawaii under contract from NASA.

1. INTRODUCTION

The Lynds 1630 (L1630) dark cloud is part of the Orion B Molecular Cloud. At a distance of approximately 450 pc, it is one of the nearest giant molecular clouds. Its mass is estimated to be more than $\sim 1 \times 10^5 M_\odot$ (Maddalena et al. 1986).

L1630 shows many signs of on-going star formation: (a) dense cores of molecular gas and high velocity outflows (Snell & Edwards 1982; Gibb & Heaton 1993; Gibb et al. 1995); (b) bright reflection nebulae (e.g., NGC 2068 and NGC 2071); (c) T Tauri stars (Herbig & Kuhi 1963; Wiramihardja et al. 1989); (d) Herbig-Haro (HH) objects, including the morphologically complex HH 24–26 (Herbig 1974; Solf 1987; Mundt, Ray, & Raga 1991; Eislöffel & Mundt 1997); (e) luminous far-infrared and submillimeter sources (Cohen et al. 1984; Cohen & Schwartz 1987; Gibb & Heaton 1993; Schwartz, Burton, & Herrmann 1997; Mitchell et al. 2001); (f) radio continuum sources (Bontemps, André, & Ward-Thompson 1995; Verdes-Montenegro & Ho 1996; Reipurth et al. 2002); and (g) dense clusters of optically obscured near-infrared sources (Strom et al. 1975; Strom, Strom, & Vrba 1976). The number density of young stars in L1630, 450 pc^{-3} , is comparable with that of the ρ Ophiuchus star-forming region (Lada et al. 1991).

Starting with the work of the Stroms, L1630 has been studied in ever increasing detail at infrared wavelengths. Particular attention has been focused recently on its many outflows and HH features. Evidence for emission in the $2 \mu\text{m}$ near-infrared lines of H_2 from parsec-scale HH flows and jets has been presented by Zealey et al. (1992), and more extensively by Davis et al. (1997) and Chrysostomou et al. (2000). Images of HH 24 in narrow emission lines at optical and infrared wavelengths trace out at least three intersecting, collimated, bipolar flows (e.g., Mundt et al. 1991: Fig. 17–19; Davis et al. 1997: Fig. 2). The flows emanate from the vicinity of HH 24B, at the location of the bright near-infrared sources SSV 63E and SSV 63W. Both objects are presumed from their steep spectral energy distributions to be Class I protostars (Cohen et al. 1984), that is, they are in a very early stage of evolution preceding the T Tauri star (TTS) or so-called Class II phase, and in the process of actively accreting material from their protostellar disks. The dynamical age of HH 24 is of the order of $\sim 10^4$ yr (Eislöffel & Mundt 1997; Snell & Edwards 1982), which implies that the Class I objects powering those flows must be very young, and also in a very short-lived phase of evolution.

In the past, the bright HH 24A knot was interpreted as the “working surface” or bow shock for one of those outflows (Mundt et al. 1991; Solf 1987), but it is now recognized (e.g., Eislöffel & Mundt 1997) to be the terminus of an independent outflow, which originates in a region immediately to the southwest, at the location of a deeply embedded Class 0 protostar, HH 24-MMS. Class 0 objects like HH 24-MMS represent the main accretion phase for protostars and are extremely rare because their lifetimes are so short. HH 24-MMS is observed directly at near-infrared wavelengths only in shocked H_2 (Bontemps, Ward-Thompson, & André 1996; Davis et al. 2002). It was discovered as a bright source at submillimeter and radio wavelengths (Chini et al. 1993; Ward-Thompson et al. 1995; Bontemps et al. 1995). Greybody fits suggest a color temperature of 20 K and

a total luminosity of \sim 5–20 L_\odot , of which $\sim 2.5 L_\odot$ originates from an unresolved and possibly disk-like central source (Ward-Thompson et al. 1995). The compact source is surrounded by a much more extended envelope, from which it is most likely accreting material at a very high rate (Chandler et al. 1995b). The detection of an H_2 jet, blue-shifted CO emission (Bontemps et al. 1996), and indications of disk structure suggest that HH 24-MMS, even at its remarkably young age, has already begun to drive a powerful collimated outflow into the surrounding molecular cloud. Various theories and mechanisms have been advanced in the past to explain such highly focused (and frequently bipolar) jets. In the class of magnetic models, for example, it has been proposed that the outflow is confined and driven by interactions between the magnetosphere of the protostar and the primordial field that threads its accretion disk (e.g., Shu et al. 1994).

South of HH 24, high resolution radio, millimeter, and submillimeter maps have revealed a number of strong molecular peaks and bipolar outflows in the proximity of HH 25 and HH 26 (Gibb & Heaton 1993; Gibb et al. 1995; Gibb & Davis 1998). The surrounding areas have been extensively mapped in the $v = 1 - 0 S(1)$ line of H_2 at $2 \mu\text{m}$ (Davis et al. 1997; Chrysostomou et al. 2000; Davis et al. 2002). A Class 0 object, HH 25-MMS, was discovered $10''$ south of the optically-visible knot HH 25A as both a 1.3-mm and a 3.6-cm source (Bontemps et al. 1995). Strong 450 and $850 \mu\text{m}$ continuum emission has been observed from the same location (Mitchell et al. 2001; Phillips, Gibb, & Little 2000). The brightest near-infrared objects in the vicinity of HH 25–26 are SSV 59, SSV 60, and HH 26-IR (Strom et al. 1976; Davis et al. 1997). None of the three has been shown conclusively to be the origin of a large-scale flow, although the weight of the evidence for HH 26 (in particular, the discovery of a compact H_2 jet: Davis et al. 2002) now points most convincingly to HH 26-IR. The latter, as well as SSV 59, is generally regarded as a Class I protostar (e.g., Bontemps et al. 1995, Davis et al. 2002). The status of SSV 60 is unknown; unlike the other two sources, it is associated with neither a submillimeter peak (Lis, Menten, & Zylka 1999; Mitchell et al. 2001; Phillips et al. 2001) nor a molecular core (e.g., Torrelles et al. 1989; Gibb & Heaton 1993).

The same process that drives the outflows and jets of Young Stellar Objects (YSOs) is expected to result in the repeated shearing and reconnection of the magnetic field lines that attach such a star to its circumstellar disk, and thereby to generate a substantial amount of X-ray emission (Hayashi, Shibata, & Matsumoto 1996; Shu et al. 1997; Goodson, Winglee, & Böhm 1997). The numerical simulations of Hayashi et al. and Goodson et al. in particular demonstrated that as a consequence of reconnection events some of the magnetically entrapped gas that is close to an accreting YSO (not necessarily its outflowing jet) will reach temperatures as high as 100 MK and will be flung outwards, away from the star. Such high temperatures should give rise to hard X-ray spectra. X-ray emission at equally high temperatures can also be produced in an accretion shock at the footpoints of the magnetic field, where infalling material from the disk streams down onto the surface of the forming star (Uchida & Shibata 1984). The HH 24–26 region was observed in X-rays with ASCA for a net exposure time of 30 kiloseconds (ks) by Ozawa et al. (1999). The strongest source in the soft X-ray band (0.7–2.0 keV) in that observation was SSV 61, a T Tauri star (TTS) which is embedded in an unusual patch of nebulosity situated mid-way on the sky between HH 24 and

HH 25–26 (e.g., Scarott, Gledhill, & Warren-Smith 1987). Strom et al. (1975) classified the star as an M2–M4 giant from image-tube spectra. A CCD spectrum of SSV 61, kindly made available to us by G. Herbig, exhibits H α emission and Li I λ 6707 absorption equivalent widths that are typical of the class of weak-lined T Tauri stars (wTTs), $\text{EW}(\text{H}\alpha) = -5$ Å and $\text{EW}(\text{Li I}) = 480$ mÅ (cf. Walter 1986; Martín et al. 1994). The brightest emission in the hard ASCA band (2.0–8.0 keV) is located north of SSV 61, in the vicinity of HH 24. The high-energy peak lies nearest SSV 63, but cannot be identified unambiguously with either of its infrared components due to the low spatial resolution of ASCA. Ozawa et al. noted the great difficulty of separating the X-ray flux of SSV 63 from that of SSV 61, given their offset of just 1.8, at roughly the half-power radius of ASCA. The quiescent luminosity $L_x \simeq 10^{32}$ ergs s $^{-1}$ they derive for SSV 63 places it above the top end of the range thus far observed for all but a few Class I objects, by factors of 50–100 (Carkner, Kozak, & Feigelson 1998; Preibisch, Neuhäuser, & Stanke 1998). Whether SSV 63 is truly one of the most X-ray luminous YSOs in the sky, however, has awaited confirmation from high resolution imaging that resolves not only SSV 61 from SSV 63, but also the individual infrared components of SSV 63 itself. That task, including the requisite high precision astrometry, has now been accomplished by the *Chandra* observations reported here.

As for the Class 0 sources in L1630, Ozawa et al. found no sign of X-ray emission at the position of HH 24-MMS, located in the saddle between the soft and hard X-ray peaks in their image, nor any emission at the position of HH 25-MMS, which was also in the ASCA field of view. Their 3σ upper limit of $L_x \lesssim 1.2 \times 10^{31}$ ergs s $^{-1}$ is not a stringent limit on the emission, however, since YSOs elsewhere in Orion and in other star forming regions have been detected at much fainter levels, $L_x \simeq \text{few} \times 10^{30}$ ergs s $^{-1}$ (e.g., Feigelson et al. 2002; Imanishi, Koyama, & Tsuboi 2001). Using the *Chandra Observatory*, we have undertaken a far more sensitive search for the onset of X-ray emission in the Class 0 objects within the L1630 cloud. Our objective was to establish an evolutionary progression in X-ray properties within a single cloud, and to examine the possible relationship between protostellar X rays, accretion disks, magnetically confined jets, and large-scale molecular outflows. Taking advantage of the lower background, greater sensitivity, and unsurpassed spatial resolution of *Chandra*, we are now able to set a 10 times smaller bound on possible X-ray emission from the three established Class 0 protostars in the L1630 cloud, HH 24-MMS, HH 25-MMS, and LBS 17-H.

2. OBSERVATIONS and RESULTS

2.1. The X-Ray Imaging-Spectroscopy

L1630 was observed with the Advanced CCD Imaging Spectrometer array (ACIS: Garmire et al. 2002) on the *Chandra X-Ray Observatory* for a net exposure time (livetime) of 62.8 ks. The date of observation was 14–15 November 2002. All six detector chips of the ACIS-S camera, S0–S5, were activated during the observation. The aim point of the observation was chosen to place SSV 61

close to the center of the back-illuminated S3 chip and to put HH 24 and HH 25–26 on the same device within a few arcminutes of the optical axis of the telescope, thereby ensuring the best optical performance for our highest priority targets within the ACIS field of view. The roll angle of the observation, 61° , was selected to position the NGC 2068 reflection nebula, located to the northeast of HH 24–26, on the back-illuminated S1 chip of the detector array and the Class 0 object, NGC 2068/LBS 17-H (Gibb & Little 2000), on the adjacent, front-illuminated S2 chip. The majority of the field of view is shown in Fig. 1, superposed on the red image of the Digitized Sky Survey of the Space Telescope Science Institute (DSS). The approximate locations of HH objects in the neighboring areas are marked, as are the positions of the two dozen X-ray sources we have detected in our *Chandra* observation.

To analyze the *Chandra* image, we initially filtered the Level-2 X-ray event file provided by the pipeline data processing system, retaining only the photon events that were assigned ASCA grades 0, 2, 3, 4, and 6 and that were within the broad (0.5–10) keV energy band in which the ACIS detector has its highest response and the background radiation is at its lowest levels. Subsequent steps in the analysis, including photometry and astrometry, were carried out following various data analysis threads within CIAO, the interactive *Chandra* data analysis package. For source detection, we applied the CELLDTECT sliding-cell detection algorithm. Twenty-five sources, all of them point-like, were found on the six chips. To extract X-ray counts for each source, we used the DMEXTRACT tool. We employed a circular extraction region with a radius of 10 pixels ($r = 5''$) to measure the brightness of sources located within $7'$ of the optical axis of the telescope, a radius twice as large for sources more than $7'$ off-axis, and an annulus at least 10 times as large to evaluate the background emission.

The results of the photometry are given in Table 1. Listed there are the right ascension and declination (J2000) of each source, its off-axis angle, the net source counts extracted within the 0.5–10 keV band, and the statistical errors in the source counts. In the final column we tabulate the count rate for the effective exposure time of each source, which takes account of the variations in the sensitivity of the camera across the field of view, as indicated by our exposure map calculations. The adjustments are negligible for the nearly on-axis sources on the S3 chip that are the main interest of the present study, but may be as great as 50% for the few objects that are located either near the edge of a detector chip or else far away from the optical axis of the telescope. We also list possible optical and infrared counterparts, which were found by cross-matching the X-ray coordinates with entries in the SIMBAD database and by visual comparison with red images from the DSS as well as infrared images from the 2MASS sky survey. The identifications include several $\text{H}\alpha$ emitters (Herbig & Kuhi 1963), named infrared sources (Strom et al. 1976), anonymous near-infrared objects from the 2MASS survey, and entries in the *Hubble Space Telescope* Guide Star Catalog-II (identified here with the prefix of S). The correspondence of each X-ray and optical/infrared position is within $1''$ ($= 2$ ACIS pixels) or less. The position of X-ray source no. 4 coincides with the location of a previously known non-thermal, extragalactic radio source (Bontemps et al. 1995; Anglada et al. 1998). A search of the NASA/IPAC Extragalactic Database (NED) turned up no other background

objects in the ACIS field of view.

SSV 63 is resolved into three separate X-ray components, which correspond to the VLA 3.6-cm radio positions of SSV 63E, 63W, and 63NE (Reipurth et al. 2002). An overlay of the radio source positions on the 2–8 keV hard-band X-ray image from *Chandra* is shown in Fig. 2. Within the uncertainties in the absolute coordinates of the radio and infrared sources (see Table 1 of Bontemps et al. 1995), and the astrometric error in *Chandra* observations (nominally 1 pixel, or 0''.5, for positions close to the optical axis of the telescope²), the X-ray centroids coincide with the infrared counterpart of SSV 63E and the brighter, southern, infrared component of SSV 63W. The fainter infrared component of SSV 63W, located 2'' farther north (see Fig. 2 of Davis et al. 2002), appears dark in X rays. SSV 63NE is a source of both radio emission and X-ray emission, but has no near-infrared counterpart (as we will show below in §2.2). If not a distant background object, it may qualify on that basis as an extreme Class I or possible Class 0 YSO. All three components of SSV 63 have hard X-ray spectral indices: 96% of the X-ray photons detected from SSV 63W have pulse-height energies greater than 2 keV, while all of those detected for SSV 63E and NE have energies of 2 keV or more. We performed individual χ^2 timing analyses for the three X-ray components, using the XRONOS software package from the High Energy Astrophysics Science Archive Research Center (HEASARC) of the NASA/Goddard Space Flight Center. We found no indication of variability on timescales of 6 ks or longer, certainly nothing comparable in amplitude or duration to the order-of-magnitude outburst in X-ray flux recorded by ASCA (Ozawa et al. 1999). The X-ray count rates listed in Table 1 therefore likely correspond to the quiescent activity levels of those sources. Changes on timescales shorter than 6 ks were not investigated owing to the faintness of the sources.

The strongest X-ray source in the *Chandra* field of view was the wTTS, SSV 61, for which we accumulated very nearly 13,000 counts in the 0.5–10 keV bandpass. The X-ray light curve of SSV 61 was stable throughout the entire observation; various χ^2 tests performed with XRONOS found no evidence of variability on timescales greater than 300 s. To analyze the X-ray spectrum of SSV 61, we used the HEASARC XSPEC spectral analysis package in order to fit simple multi-temperature thermal plasma models to the pulse height distribution of the extracted photons. The quality of the fit was determined by χ^2 minimization. In the calculations, we removed a small (< 1%) contribution of emission from the background and also updated the instrumental response function to compensate for the on-orbit decline in the low-energy sensitivity of the ACIS detectors³.

In terms of the reduced χ^2 value of the fit, no satisfactory model was found. Typical of the results we obtained are the following parameters for a two-temperature, reduced-metal MEKAL fit (Mewe, Kaastra, & Liedahl 1995), which we matched to the observed counts in the 0.5–7.0 keV pulse-height energy channels: reduced $\chi^2_{(\nu=254)} = 1.45$; $kT_1 = 1.23 \pm 0.06$ keV, $kT_2 = 10 \pm 3$ keV; one-

²<http://cxc.harvard.edu/cal/ASPECT/celmon/>

³http://cxc.harvard.edu/cal/Acis/Cal_prods/qeDeg/index.html

third solar elemental abundance, $Z = 0.33 \pm 0.10$; hydrogen column density, $N_H = 0.30 \pm 0.02 \times 10^{22} \text{ cm}^{-2}$; volume emission measure, $\log EM = 54.66 \pm 0.05$, three-quarters of which are due to the high-temperature component; broadband flux at Earth, $f_x(0.3\text{--}10 \text{ keV}) = 2.25 \pm 0.09 \times 10^{-12} \text{ ergs cm}^{-2} \text{ s}^{-1}$; and intrinsic (absorption-corrected) X-ray luminosity for an assumed distance of 450 pc, $L_x(0.3\text{--}10 \text{ keV}) = 7.20 \times 10^{31} \text{ ergs s}^{-1}$. Here, $\nu (= 254)$ is the number of degrees of freedom in the model. Closely similar fits were obtained with both the XSPEC PILEUP model (see Davis 2001), which we used to account for the $\sim 10\%$ pileup fraction in our spectrum of SSV 61, and also the APEC plasma emission code described by Smith et al. (2001). An example of an APEC model fit is shown in Fig. 3. Except for a few possible camera artifacts, the largest residuals in all the model fits are attributable to excess emission in the observed spectrum near photon energies of 1 keV. The apparent excess may be due to lines of Ne IX and X or to inner shell transitions of high ionization stages of Fe. A similar excess has also been observed in the ACIS spectra of pre-main sequence stars in other star-forming regions, e.g., Orion and ρ Ophiuchus (Feigelson et al. 2002; Imanishi, Tsujimoto, & Koyama 2002).

An evaluation of the intrinsic 0.3–10 keV brightness of SSV 61 for a variety of XSPEC models produced very nearly the same results for the X-ray flux and for the luminosity. The various models also yielded closely similar amounts for the hydrogen column density. From the models and the empirical relation of Bohlin, Savage, & Drake (1978), we infer a visual extinction of $A_v = 1.6$ mag. Our estimate, drawn from the *Chandra* spectrum of SSV 61, is a factor of four less than the extinction Ozawa et al. (1999) derived from their ASCA observation, but is consistent with the conclusion reached by Strom et al. (1975) on the basis of infrared colors that the foreground reddening to this star is relatively small. Infrared spectroscopy (discussed below) further confirms the low extinction for this star.

The three X-ray sources identified with SSV 63 were too faint for detailed spectral model fitting, and so we limited ourselves to a few simple models of the strongest component, SSV 63W. For that source we chose an isothermal, one temperature (1-T) MEKAL model, constrained it to a sub-solar abundance of $Z = 0.5$, and allowed XSPEC to search for values of N_H and kT that minimized the χ^2 of the fit. The best-fit values derived by XSPEC were $N_H = 9.0 \pm 1.8 \times 10^{22} \text{ cm}^{-2}$ (equivalent to 48 mag of visible extinction) and $kT = 1.62 \pm 0.41 \text{ keV}$. The resulting hydrogen column density is at the low end of the range of values deduced by Ozawa et al. (1999), while our temperature is a factor of 3 lower than their best-fit value for a quiescent interlude in the ASCA observation. A reddened bremsstrahlung model, which we chose as an alternative fit, produced a similar χ^2 , temperature, and N_H as the MEKAL model. Both models, the MEKAL and the bremsstrahlung, yielded a comparable 0.3–10 keV flux and absorption-corrected luminosity for SSV 63W: $f_x \approx 5.3 \pm 0.5 \times 10^{-14} \text{ ergs cm}^{-2} \text{ s}^{-1}$ and $L_x \approx 1.4 \times 10^{31} \text{ ergs s}^{-1}$. Raising the temperature to a fixed value of $kT = 5 \text{ keV}$ for consistency with the ASCA result reduced the column density to $N_H = 5.2 \pm 0.6 \times 10^{22} \text{ cm}^{-2}$, corresponding to an extinction of $A_v = 27$ mag, but yielded a much poorer fit to the *Chandra* pulse-height spectrum in terms of its χ^2 value.

No model analysis was possible for the two remaining components of SSV 63, given the small

numbers of counts recorded for them during our *Chandra* observation. To estimate X-ray luminosities for those sources, we scaled from SSV 63W in proportion to the background-adjusted number of counts detected for each source. In doing so, we implicitly assumed that the optimal XSPEC models of SSV 63E and SSV 63NE would yield the same parameters as the best-fitting model for SSV 63W. Our normalization procedure is equivalent to using a counts-to-energy conversion factor (ECF) of 2.00×10^{-11} ergs cm $^{-2}$ s $^{-1}$ per count s $^{-1}$ for the X-ray flux observed at Earth, and 5.40×10^{33} ergs s $^{-1}$ per count s $^{-1}$ for the extinction-corrected broadband luminosity.⁴ Anticipating the results of §3.2, we note that sub-millimeter observations of L1630 corroborate the high extinction value provided by our X-ray analysis of SSV 63W. On the other hand, spectroscopy of the infrared ice band in the direction of SSV 63E and W (discussed in §2.3) suggests that the foreground extinction towards both sources may be only half as large, $A_v \approx 20$ mags. The apparent discrepancy raises the possibility that the X-ray sources may be more deeply obscured than are the near-infrared sources, reflecting, perhaps, an anomalous gas-to-dust ratio along the line of sight.

The X-ray luminosities for SSV 61 and SSV 63 are summarized in Table 2. Our L_x value for SSV 61 is 15% higher than the ASCA result of Ozawa et al. (1999) but lies substantially above the high end of the range found in an extensive survey of wTTS in Taurus by ROSAT (Neuhäuser 1997) and is well above the range of X-ray luminosities measured by *Chandra* for low-mass stars in both Ophiuchus (Imanishi et al. 2001) and the Orion Nebula Cluster (Feigelson et al. 2003). Our L_x value for SSV 63W falls near the top end of those three luminosity distributions, while the values for the two other detected Class I YSOs, SSV 63E and 63NE, are in the top quartile of each range. Also listed in the table are upper limits on the X-ray emission of the near-infrared objects SSV 60 and 59, the former lying between HH 25C and 25D along the curving ribbon of emission knots that define HH 25 (being closer to D), the latter lying just north of HH 26A. The upper limits on the count rates given in the table are three times the Poisson uncertainties in the total counts (uncorrected for background emission) measured through a 10'' diameter circular detection cell, which we centered on the respective 2MASS positions listed in the second and third columns of the table. Based on Eqn. 10 in Gehrels (1986), the significance level of these upper limits corresponds to 2σ , i.e., to a confidence level of 0.95. The upper limits obtained for a smaller 5'' diameter detection cell, which still encircles more than 95% of the energy in the *Chandra* point spread function, are ~ 0.23 dex lower at a confidence level of 0.95, in accordance with either Gehrels (1986) or the Bayesian approach of Kraft, Burrows, & Nousek (1991), but may be subject to a somewhat greater uncertainty due to the imprecision of the infrared coordinates of both objects. For lack of a more compelling choice, the conversion from count rate to luminosity in Table 2 is based on the ECF derived from our XSPEC modelling of SSV 63W. The upper limits cited on the luminosity assume both objects lie at a distance of 450 pc within the L1630 cloud, which may not be true for SSV 60,

⁴The ECF based on our spectral fits to SSV 61 would be 0.90×10^{-11} ergs cm $^{-2}$ s $^{-1}$ per count s $^{-1}$ for the X-ray flux and 2.85×10^{32} ergs s $^{-1}$ per count s $^{-1}$ for the luminosity. These smaller conversion factors may be appropriate to other lightly reddened, visible stars that are listed in Table 1 along with SSV 61 but do not apply to such heavily reddened sources as SSV 63.

as we discuss further in §2.3.

In similar fashion, we derived 2σ upper limits on the possible X-ray emission from the three Class 0 objects in the L1630 cloud, HH 24-MMS, HH 25-MMS, and LBS 17-H. Those results are also given in Table 2. In each case, the detection cell was centered at the known long-wavelength or radio position of the object. The J2000 coordinates of HH 24-MMS and HH 25-MMS were precessed from the B1950 VLA positions of Bontemps et al. (1995) and Gibb (1999); those of LBS 17-H were precessed from the B1950 location of the peak in the $450\mu\text{m}$ dust continuum map of Phillips et al. (2001). Finally, we list an upper limit for our X-ray non-detection of HH 26-IR, the possible driving source for the HH 26 outflow (Schwartz et al. 1997, wherein the object is known as IRS 4). The B1950 location for that source was taken from the discovery paper of Davis et al. (1997) and precessed to an equinox of J2000.

2.2. The Infrared Imaging

Two sets of JHK near-infrared images were obtained of the HH 24–26 region on 18 November 2002, using the University of Hawaii QUIRC HgCdTe camera array (Hodapp et al. 1996). The instrument was mounted at the f/10 Cassegrain focus of the 2.2-m telescope on Mauna Kea. The image scale was $0''.19\text{ pixel}^{-1}$, the field of view was $3''.2$. One set of images was centered on SSV 63 and HH 24, the other mid-way between SSV 59 and 60 in the vicinity of HH 25–26. At both locations, a sequence of 3×10 s exposures was obtained at each of 20 separate positions, offset by $10''$ in right ascension and declination, to produce a heavily sampled dither-pattern. The same cycle was repeated in each of the three filter bands. We alternated the observations of both HH fields with similar integrations on a pair of flanking fields $150''$ E and W, from which the bright stars were subsequently removed in order to create suitable sky frames. Flat-field frames were created by median-averaging observations of the 2.2-m dome under illumination by incandescent lamps. In the reductions, the dithered HH frames were flat-fielded and sky-subtracted, then aligned by cross-matching the positions of bright stars to form an enlarged median-averaged mosaic. The cumulative exposure time in the center of the final co-added image in each filter is ~ 500 s. Taking into account the intermittent, non-photometric observing conditions, we estimate brightness limits of 20.9 mags, 20.1 mags, and 18.5 mags in J , H , and K , respectively. The typical seeing in the course of the observations was $0''.5$ in K (FWHM). However, the PSF of stellar images in the co-added data proved to be somewhat broader than this, and also slightly distorted, as a result of a misalignment of the primary mirror of the 2.2-m telescope.

Our images of HH 24 in the three colors are shown in Fig. 4. The positions of the individual components of SSV 63, as listed in Table 2, are marked on the J -band image. We have also identified the expected locations of the two most prominent HH emission knots, 24A and 24B. The position from Table 2 of the Class 0 object, HH 24-MMS, is also noted. That source is faintly visible in the K image, the bandpass of which includes a number of H_2 lines, and is also very weakly present in the H image, whose bandpass includes $[\text{Fe II}] 1.64\mu\text{m}$, a low-excitation emission line that is observed

in the jets of some HH objects (e.g., Reipurth et al. 2000). As noted earlier, the elongated jet associated with HH 24-MMS is very prominent in the continuum-subtracted, narrow-band H₂ images of Bontemps et al. (1996, their Fig. 1a) and Davis et al. (1997, their Fig. 2), and also in the Fabry-Perot image of Davis et al. (2002, their Fig. 3). The N–S components of SSV 63W are cleanly separated in our *J*-band image, but are heavily exposed in the longer-wavelength images, as is true of SSV 63E. An extended halo around the latter component, pointing westward, becomes increasingly evident with increasing wavelength. Contrary to previous reports (Moneti & Reipurth 1995; Terquem et al. 1999), we see no evidence to suggest this star is double or that the emission peak in *H* lies 1'' west of the peak in *K*. In our images, there is no shift in the position of the peak with color to a limit of 1 pixel or 0''.2.

The coordinates of the radio and X-ray source SSV 63NE place it adjacent to two very red patches of nebulosity known from earlier work (e.g., Zealey et al. 1992). A false-color image that combines the three separate panels of Fig. 4 exhibits a noticeable gradient in color from W to E, possibly originating at SSV 63E. The variation in color suggests that both patches of infrared nebulosity may be illuminated by an embedded source to the west, either the Class I source, SSV 63E, which Scarrott et al. (1987) proposed as the illuminating source for the diffuse optical nebulosity of HH 24, or else a much more deeply embedded infrared object at the location of 63NE. The radio and X-ray coordinates of SSV 63NE coincide to within 3''.3 with the position for the predicted but unobserved “Jet G Star” of Jones et al. (1987), which those authors proposed to be the driving source of the HH 24G outflow (see also Mundt et al. 1991, in particular the highly detailed [S II] image in their Fig. 17). The absence in Fig. 4 of any obvious point source at the same location to a limit of *K* = 18.5 mag implies that this star, presuming it does exist, lies exceedingly deep within the molecular cloud. Given our detection of X-ray emission at the radio position, there can be no doubt that SSV 63NE, if it is a protostar of Class 0, has already evolved past the stage of isothermal collapse. Submillimeter maps of the region obtained with the SCUBA bolometer array on the JCMT (Phillips et al. 2001; Mitchell et al. 2001) show extended emission at the position of SSV 63 but are unable to resolve 63NE from the two other radio components, 63E and 63W. Consequently, although it seems quite likely that SSV 63NE is a bona fide YSO, its exact status is not yet entirely settled.

Our infrared images of the southern region containing HH 25 and 26 are presented in Fig. 5. Again, for orientation, the positions of the notable objects in the field of view are marked. The Class 0 protostar, HH 25-MMS, is invisible in both the *J* and *H* images, although a hint of emission (presumably from ro-vibrational lines of H₂) can be seen at the radio position of this object in the *K*-band image. HH 25A and SSV 59 are both immersed in nebulosity. Nebulae of similar appearance have been seen in high resolution images of other embedded protostars, e.g., HL Tau (Close et al. 1997, especially their Figs. 2 and 4) and interpreted as the outline of bipolar cavities. SSV 59 has been classified as a Class I object. No star has been observed before at the location of HH 25A at optical wavelengths. However, this HH knot is uncommonly bright in the *J* and *H* frames in Fig. 5 to be merely the “working surface” of a high-velocity outflow from HH 25-MMS, located

immediately to the south. Our underexposed 1.9–2.5 μm infrared spectrum of HH 25A displays an array of very strong emission lines of H₂, which likely arise from shock-heated gas, but no spectral signatures of an underlying star.

A very red, compact emission knot is observed at the location of HH 25C, in approximate alignment with HH 25A, SSV 60, and HH 25D. As mentioned earlier, we believe SSV 60 is a heavily reddened background giant, not a member of L1630. No other plausible candidate for the exciting source of HH 25 is revealed by our images.

2.3. The Infrared Spectroscopy

Infrared spectra of SSV 59, 60, 61, 63E, 63W (both the north and south components combined), and HH 26-IR were acquired with the SpeX cross-dispersed, medium-resolution spectrograph (Rayner et al. 2003) at the 3.0-m NASA IRTF telescope on Mauna Kea on 3 January and 1–3 February 2003. SpeX covers the full wavelength range from 0.8 to 5.5 μm in two grating settings. We observed each source in the 1.9–4.2 μm wavelength region, using the LXD setting; the two brightest objects, SSV 60 and 61, were also observed in the 0.8–2.4 μm region with the SXD setting. Observing conditions were photometric and dry throughout, with typical seeing values near 0''.5 FWHM (measured in *K*-band). Slit widths of 0''.3 and 0''.5 at the short- and long-wavelength settings provided a nominal spectral resolving power, $\lambda/\Delta\lambda$, of 2000 and 1500, respectively. Our on-source integration times ranged from 300 to 1200 s and resulted in signal-to-noise ratios of 20–50 in both the *K* and *L* bands.

Each observing sequence began with a nearby (less than 0.05 difference in airmass) A0 V standard star, moved to the target object, and finished with a set of internal calibration spectra. To cancel the sky background, we observed in the conventional way by nodding along the 15''-long slit. The data were reduced with the SPEXTOOL⁵ software package (see Cushing et al. 2003 for details). Spectra were extracted using a 1''.2 aperture along the slit, corrected for telluric features, and calibrated in flux by means of the standard star spectra according to the techniques that have been described by Vacca, Cushing, & Rayner (2003). The processed spectra are shown in Fig. 6, where they are plotted on a logarithmic flux scale.

The infrared continua of SSV 60 and 61 come to a peak blueward of the *K*-band, near 1.9 and 1.5 μm , respectively. Absorption lines from a variety of neutral and ionized metals, including Ca I, Fe I, Mg II, Al I, Ti I, and Na I, can be seen in the spectra of both stars. No emission lines are observed in the spectrum of SSV 60. The Br α line of H I at 4.05 μm appears in emission in the spectrum of SSV 61; its equivalent width is entirely consistent with the observed strength of H α , Case B recombination, and very little foreground reddening. Both spectra exhibit deep absorption bands from the first overtone ro-vibrational transitions of CO near 2.3–2.5 μm . Assuming the

⁵<http://irtfweb.ifa.hawaii.edu/Facility/spe/>

observed atomic and molecular features are photospheric in origin, we have used their relative strengths to estimate the spectral type and luminosity class of the underlying stars in the manner described by Kleinmann & Hall (1986), Hodapp & Deane (1993), and Greene & Meyer (1995). Here we have adopted Aspin’s (2003) formulation, in which an atomic index formed by the sum of the equivalent widths of the Na I doublet at $2.21\text{ }\mu\text{m}$ and the Ca I triplet at $2.26\text{ }\mu\text{m}$ is compared to a molecular index represented by the equivalent width of the $v=2-0$ CO bandhead at $2.29\text{ }\mu\text{m}$ (see Fig. 7). According to their atomic and molecular index values, SSV 60 (4.2 \AA , 10.0 \AA) is definitely a giant, whereas SSV 61 (5.9 \AA , 9.4 \AA) is intermediate to a dwarf and giant (a not uncommon finding for a TTS). We have combined the spectral indices, the strengths of the various photospheric absorption lines of the metals, the deep CO bandheads, and the general continuum shapes to estimate spectral classifications of K5–M0 III for SSV 60 and M0–M2 III/V for SSV 61. Those spectral types, resting solely on the infrared spectra, are consistent with the locations of both stars in a ($J - H$, $H - K$) color-color plot based on their 2MASS photometry, and also with the effective temperatures we have derived following the procedure of Greene & Meyer (1995), which makes use not only of the absorption line strengths but the broadband colors as well. The latter technique provides, among other things, an estimate of the fraction of excess light from veiling continuum emission, which we find to be constrained to low values for both stars ($r_H, r_K < 0.15$ at H and K).

The association of SSV 61 with the L1630 molecular cloud is hardly in question, but the same cannot be said for SSV 60. With its bright, attendant nebula, SSV 61 would be a rare star indeed to be in the far foreground of this region, while the absence of any ice absorption at $3.08\text{ }\mu\text{m}$ in its infrared spectrum (Fig. 6) argues against the likelihood it lies far behind the molecular cloud at a very considerable distance from Earth. For an early M giant, SSV 60 is clearly much more heavily absorbed than SSV 61, as is apparent from its spectral energy distribution shortward of $2\text{ }\mu\text{m}$ and its strong ice absorption band. The broad ice feature is common to the spectra of other sources which are either background to or deeply embedded within molecular clouds, where the ice has condensed onto dust grains but not undergone significant processing at high temperature (Smith, Sellgren, & Tokunaga 1989). For SSV 60, the optical depth at band center, $\tau_{ice} = 0.96$, leads (according to the results of Whittet et al. 1988) to an optical extinction of roughly $A_v \approx 17$ mag. Such heavy extinction is not to be found in the foreground to L1630. On the other hand, SSV 60 shows none of the signposts of youth or activity that are expected for an embedded Class I protostar—no X-ray emission, no high velocity outflow or jet in CO or H₂, no far infrared or sub-mm emission. We conclude, therefore, that SSV 60 is a background giant star that is unconnected either with L1630 or with HH 25, on which it is apparently coincidentally projected.

The strong red continua and deep ice bands of HH 26-IR, SSV 59, 63E, and 63W, on the other hand, suggest that each of those objects is deeply embedded within the L1630 cloud. Their observed ice-band optical depths range from $\tau_{ice} = 0.8$ (for HH 26-IR) to $\tau_{ice} = 1.3$ (for SSV 63E and W), corresponding to approximate A_v values of 10 to 20 mags. At close inspection, the ice band spectra of SSV 59 and 63E also show a broad, shallow depression near $3.45\text{ }\mu\text{m}$. That feature, according to Smith et al. (1989), can be identified with the C–H stretching modes of hydrocarbons

(in the CH_2 and CH_3 subgroups). Emission lines of H I are visible in the spectra of all four objects, including $\text{Br}\alpha$ $4.05\,\mu\text{m}$, $\text{Br}\gamma$ $2.17\,\mu\text{m}$, and (in the case of SSV 63E) $n=8-5$ $\text{Pf}\gamma$ $3.74\,\mu\text{m}$. The emission is a clear indication of ionized gas in the close vicinity of each star, but whether the warm gas is inflowing or outflowing is a matter of continuing debate (e.g., Najita, Carr, & Tokunaga 1996; Folha & Emerson 2001). There are no signs in our spectra of any photospheric absorption lines, which we suspect may be hidden beneath a large continuum veiling flux. Emission lines from ro-vibrational transitions of H_2 are present throughout the K -band spectra of SSV 63W and HH 26-IR, the $2.12\,\mu\text{m}$ $1 - 0\,S(1)$ line being the strongest (Fig. 8). The same lines are often observed in the spectra of Class I objects (Greene & Lada 1996). They are also commonly observed in the spectra of high velocity outflows (e.g., Gredel 1994, 1996) and have been attributed to excited H_2 molecules that form behind shocks which arise as jet material collides with the ambient gas in a cloud (Garden, Russell, & Burton 1990). The H_2 emission in our spectral images does not appear to be spatially extended in a N–S direction along the slit. However, it has already been shown by Davis et al. (2002) that the H_2 emission of HH 26-IR has a modest extension along its jet in the NE–SW direction.

The K -band spectra of SSV 59, 63E, and HH 26-IR (Fig. 8) display the first overtone ro-vibrational CO bands in emission. Various explanations have been offered for the CO lines: they may be formed in the innermost portion of a Keplerian disk or in the neutral component of a stellar wind or outflow (Carr 1989; Chandler, Carlstrom, & Scoville 1995a; Najita et al. 1996). Alternatively, the emission may be produced by accretion of disk material onto the central star via a magnetic “funnel flow” (Martin 1997; see, however, Najita et al. 2003). In any case, Biscaya et al. (1997) have demonstrated that in some cases the CO bands can be highly variable, perhaps even exhibiting periodic behavior. Carr (1989), in fact, observed the CO bands of SSV 59 in absorption, whereas they are definitely in emission in our SpeX spectra, as can be readily seen from Fig. 8.

3. DISCUSSION

3.1. The Class 0 Sources

We detected X rays from none of the three Class 0 YSOs within the *Chandra* field of view. Two of those embedded objects, HH 24-MMS and HH 25-MMS, are continuum radio sources and therefore must have a component of ionized gas; the third object, LBS 17-H, has not been detected at radio wavelengths and hence may be in an earlier stage of evolution than the others, or else its radio emission is much more optically thick and therefore below current detection levels (Gibb 1999). The radio spectral indices of 24-MMS and 25-MMS are slightly positive (Anglada et al. 1998). The indices are compatible with thermal free-free radiation (Reynolds 1986), but do not definitively rule out a possible non-thermal gyrosynchrotron origin. We note that the spectral index for gyrosynchrotron emission is most often strongly negative but it can also be weakly positive, as for a thermal source (e.g., Güdel 2002). In the case of HH 24-MMS, the radio source is spatially

resolved (Bontemps et al. 1996; Reipurth et al. 2002). Therefore, it is almost certainly free-free emission from a warm ionized jet, although some portion of it may be thermal emission from dust (Ward-Thompson et al. 1995).

We can suggest several plausible explanations to account for the dearth of X rays from the Class 0 objects in L1630: (a) assuming the three YSOs are in the main phase of protostellar accretion, they may not yet have developed accretion shocks that are strong enough to heat infalling gas to the million degree temperatures that are needed to generate X rays, or else their magnetic fields may not be strong enough or sufficiently well organized on large scales to produce intense reconnection heating of the infalling gas; (b) alternatively, if hot gas is now present around the star, the temperature of the gas may be sufficiently low (below 1–2 MK) that it emits only a very soft spectrum of X-ray photons, which is unable to penetrate the dense envelope that surrounds the growing protostar; or (c) if there is X-ray emitting gas now present at temperatures that are high enough to form hard X rays with energies of 2–10 keV, the extinction in the surrounding envelope and cloud may be sufficiently large to absorb most (or all) of the X-ray photons and to depress the emergent radiation below levels that *Chandra* can detect.

Here we address the last possibility. Since, by definition, Class 0 protostars are especially faint at near-infrared wavelengths, we do not have *JHK* colors or IRTF spectra for the Class 0 YSOs in L1630 from which we might estimate the foreground extinction to those objects. Instead, we have estimated the line-of-sight extinction to each source by making use of the relationship between visible extinction and $850\text{ }\mu\text{m}$ brightness given by Mitchell et al. (2001), $A_v = 77S_\nu$. Applying that expression in turn to the submillimeter data for HH 24-MMS, HH 25-MMS, and LBS 17-H, we find A_v estimates of 200, 100, and 86 mags, respectively. In each case, the derived extinction is larger than the value of 48 mags we previously adopted from our XSPEC model of the *Chandra* spectrum of SSV 63W.

Given the foregoing extinction estimates, we have used the HEASARC WebPIMMS tool to predict a *Chandra* detection limit for each Class 0 YSO, computing for each one the intrinsic X-ray luminosity that yields the observed 2σ count rate limit listed in Table 2. In our simulations, we have adopted a single-temperature thermal model for the X-ray emission and assumed a normal value of the gas-to-dust ratio in order to convert the submillimeter-based A_v into a column density of N_H , following Bohlin et al. (1978). Guided by our XSPEC calculations, we have considered two different source temperatures which should bracket an adequate range of spectral hardness, $kT = 5$ keV and $kT = 2$ keV. In the high-temperature case, the tabulated count rate limits for HH 24-MMS, HH 25-MMS, and LBS 17-H correspond to 2σ detection limits in $\log L_x$ of 30.30, 30.00, and 29.75, respectively. The limits in $\log L_x$ for the low-temperature models are 0.3 dex higher. For both temperatures, the predicted luminosity limits are far less than the intrinsic L_x we derived from XSPEC models of the Class I object SSV 63W, which we detected at $\log L_x = 31.16$. To have escaped detection at that L_x , i.e., to have resulted in fewer than ~ 25 net X-ray counts in our exposure time of 63 ks, the Class 0 objects would each have to suffer more than 400 mags of extinction (or else be intrinsically very much softer X-ray sources than we have assumed). Therefore, to a very

high significance level, it appears all three Class 0 objects are intrinsically much fainter in X rays than 63W, even when the latter source is quiescent rather than flaring. The X-ray luminosity of the eastern component of SSV 63, the Class I YSO 63E, which we also detected with *Chandra*, is comparable in strength to the luminosity upper limits for the Class 0 objects. Thus, we can further assert that the Class 0 sources are fainter than 63E at the 2σ confidence level. On the other hand, because the two other established Class I objects in the same observation, SSV 59 and HH 26-IR, were not detected by *Chandra*, the X-ray brightness of individual Class I sources must have a wide range of values, even within the same star forming region. *Chandra* observations of Class I YSOs elsewhere in Orion (Tsujimoto et al. 2002) and in Ophiuchus (Imanishi et al. 2001) bear that point out. Thus, although the Class 0 objects in L1630 are clearly fainter than *some* of the Class I objects in the same cloud, they may not be fainter than *all* of them. In terms of an evolutionary trend, until more is known about the lower range of L_x values for Class I objects, and the extent to which such objects are variable, it is premature to draw any firm conclusions about whether the Class 0 sources as a group are systematically less luminous in X rays than are the more advanced Class I sources which are their descendants.

3.2. The Class I Sources

The submillimeter map of Mitchell et al. (2001) leads to an A_v estimate (47 mags) for the combined (spatially unresolved) SSV 63EW that is entirely in agreement with the extinction we have derived from our XSPEC modelling of the *Chandra* spectrum of 63W. Both the E and W infrared components of SSV 63 were detected in X rays; they are also both thermal radio emitters (Anglada et al. 1998). HH 26-IR was not detected in X rays, but may be a weak radio source according to Gibb (1999). SSV 59 is neither an X-ray source nor a radio source. However, the near-infrared spectrum of SSV 59, as well as that of HH 26-IR (Fig. 6), exhibits emission in the Brackett lines of hydrogen, implying that both objects are associated with ionized gas. The presence of a resolved H_2 jet appended to HH 26-IR (Davis et al. 2002) suggests that its radio emission may originate from the jet and be thermal in nature; the radio spectrum of SSV 59 may be optically thick and thus undetectable. It is perhaps significant that the HH filaments and knots identified with the northern Class I YSOs (the various alphabetical components of HH 24) are much more highly developed than the ones in the south (HH 25–25). This is perhaps an indication that the southern region is relatively younger and has not yet reached the age where its embedded YSOs have formed strong radio sources or possess the million degree plasma required to produce X rays.

3.3. SSV 60 and SSV 61

The weak-line T Tauri star SSV 61 is by far the brightest source in our *Chandra* image. It is also a highly variable radio source, which suggests a non-thermal origin for its radio flux (Anglada et al. 1998; Gibb 1999). As we noted in §2.3, there is very little chance of our having greatly

overestimated the distance and consequently the L_x of this star. For an assumed distance of $d = 450$ pc, the radio and X-ray luminosities of SSV 61 closely fit the $L_R - L_x$ relation for normal late-type giants, lying among the tidally locked binaries at the top end of the activity range (Drake, Simon, & Linsky 1989; Dempsey et al. 1993). This may be an indication that SSV 61 is itself a close binary. In any event, it is safe to say that the emissions of this star at radio as well as X-ray wavelengths are coronal in origin.

The near-infrared spectrum and 2MASS colors of SSV 61 in a $(J - H, H - K)$ two-color plot are consistent with those of a lightly reddened and lightly veiled early M giant star, for which $A_v < 2$ mags. However, the observed infrared magnitudes, combined with the bolometric correction for an early M giant ($K = 8.36$, $B.C.K = 2.60$ mags), imply a very high luminosity, $L_{\text{bol}} \sim 7.5L_{\odot}$, which places the star well above the stellar birthline at a logarithmic effective temperature of $\log T_{\text{eff}} = 3.5\text{--}3.6$ (Stahler 1983; Mercer-Smith, Cameron, & Epstein 1984). At that L_{bol} , the ratio of the X-ray to the bolometric luminosity of SSV 61 is at the saturation limit for the coronal X-ray emission of late-type stars, $L_x/L_{\text{bol}} \lesssim 10^{-3}$. That maximum X-ray brightness limit is well established from observations of many different kinds of late-type stars, among them wTTS like SSV 61, and so any substantial reduction in our L_{bol} estimate for SSV 61 would make it all the more difficult to understand the origin of its intense X-ray brightness. On the other hand, as one might surmise from the optical polarimetry of Scarrott et al. (1987), the 2MASS photometry of SSV 61 may be heavily contaminated by scattered light from the nebulosity that is present on all sides of the star. A large proportion of the near-infrared light of the more deeply embedded Class I objects is thought to be contributed by scattering in the protostellar envelope (Kenyon et al. 1993). In that instance the scattering adds no continuum veiling to the spectrum of the central star itself (Calvet et al. 1997). The same scattering mechanism, applied to SSV 61, would therefore be consistent with the low veiling ratio we have determined from our SpeX observation of SSV 61.

In the submillimeter map of Mitchell et al. (2001), there is an $850\mu\text{m}$ peak that coincides in position with SSV 61. The value of A_v implied by the submillimeter flux is 40 mags or more, which is inconsistent with the near absence of reddening established by the infrared colors and ice-band spectrum of SSV 61. This suggests that the cold dust producing the $850\mu\text{m}$ peak is most likely located behind SSV 61 and that the star sits in front of the cloud, possibly illuminating its front face.

In the infrared color-color plot, the 2MASS colors of SSV 60 place this star on the reddening line for late-type giants, consistent with the spectral classification we obtained from our IRTF spectrum. However, the bright near-infrared magnitudes of this star ($K = 8.44$), coupled with the large extinction implied by the deep $3\mu\text{m}$ ice band we have observed ($A_v \approx 17$), cannot be reconciled with membership in L1630. The best match we can find for the spectral type, the $(J - H, H - K)$ colors, the large amount of reddening, and the near-infrared magnitudes are for an early M background giant, which is located beyond the L1630 cloud at a distance of $d = 2.0$ kpc and with a luminosity of $L_{\text{bol}} = 600L_{\odot}$.

4. CONCLUSIONS

We have acquired a deep X-ray image of the HH 24–26 region in the L1630 cloud with the ACIS-S camera on *Chandra*, which has resulted in the detection of a number of anonymous 2MASS infrared sources and optically visible H α emission-line stars, including the X-ray luminous coronal source, the wTTS SSV 61. Also detected at what appear to be their quiescent levels of activity are two deeply embedded Class I protostars (SSV 63E and W), which have been identified in earlier work as the source of energetic molecular and ionized flows in the region. The two were blended together in an earlier detection by ASCA, but are well separated at the much higher spatial resolution of *Chandra*. Two other HH-associated Class I objects (SSV 59 and HH 26-IR) as well as three Class 0 YSOs in the same cloud (HH 24-MMS, HH 25-MMS, and LBS 17-H) were not detected. Although X-ray observations of several different star forming regions thus far reveal a striking lack of Class 0 detections, no firm conclusions can be drawn from our small sample of YSOs regarding a possible evolutionary trend in the intrinsic X-ray luminosities of the Class 0 and Class I protostars. X-ray emission was detected from a deeply embedded continuum radio source (HH 24NE), whose location within HH 24 suggests that it may be the highly obscured driving source for one of the long HH filaments in this area. The object has no visible or near-infrared counterpart, and therefore is potentially a Class 0 or extreme Class I object.

This research has made use of the SIMBAD database, operated at *CDS*, Strasbourg, France, and is based in part on observations made with the *Chandra X-Ray Observatory*. Support for this work was provided by the National Aeronautics and Space Administration through Chandra Award Number GO2-3007X issued by the *Chandra X-Ray Observatory* Center, which is operated by the Smithsonian Astrophysical Observatory for and on behalf of the National Aeronautics and Space Administration under contract NAS8-39073. The Digitized Sky Surveys (DSS) were produced at the Space Telescope Science Institute under NASA Grant NAG W-2166 and are based on photographic data obtained using the Oschin Schmidt Telescope on Palomar Mountain and the UK Schmidt Telescope with the permission of those institutions. The Guide Star Catalogue-II is a joint project of the Space Telescope Science Institute and the Osservatorio Astronomico di Torino. Space Telescope Science Institute is operated by the Association of Universities for Research in Astronomy, for the National Aeronautics and Space Administration under contract NAS5-26555. The participation of the Osservatorio Astronomico di Torino is supported by the Italian Council for Research in Astronomy. Additional support is provided by European Southern Observatory, Space Telescope European Coordinating Facility, the International GEMINI project and the European Space Agency Astrophysics Division. The Two Micron All Sky Survey (2MASS) is a joint project of the University of Massachusetts and the Infrared Processing and Analysis Center (IPAC)/California Institute of Technology, funded by the National Aeronautics and Space Administration and the National Science Foundation.

REFERENCES

Anglada, G., Villuendas, E., Estalella, R., Beltrán, M. T., Rodríguez, L. F., Torrelles, J. M., & Curiel, S. 1998, *ApJ*, 116, 2953

Aspin, C. 2003, *AJ*, 125, 1480

Biscaya, A. M., Rieke, G. H., Narayanan, G., Luhman, K. L., & Young, E. T. 1997, *ApJ*, 491, 359

Bohlin, R. C., Savage, B. D., & Drake, J. F. 1978, *ApJ*, 224, 132

Bontemps, S., André, P., & Ward-Thompson, D. 1995, *A&A*, 297, 98

Bontemps, S., Ward-Thompson, D., & André, P. 1996, *A&A*, 314, 477

Calvet, N., Hartmann, L., & Strom, S. E. 1997, *ApJ*, 481, 912

Carkner, L., Kozak, J. A., & Feigelson, E. D. 1998, *AJ*, 116, 1933

Carr, J. S. 1989, *ApJ*, 345, 522

Chandler, C. J., Carlstrom, J. E., & Scoville, N. Z. 1995a, *ApJ*, 446, 793

Chandler, C. J., Koerner, D. W., Sargent, A. I., & Wood, D. O. S. 1995b, *ApJ*, 449, L139

Chini, R., et al. 1993, *A&A*, 272, L5

Chrysostomou, A., Hobson, J., Davis, C. J., Smith, M. D., & Berndsen, A. 2000, *MNRAS*, 314, 229

Close, L. M., Roddier, F., Northcott, M. J., Roddier, C., & Graves, J. E. 1997, *ApJ*, 478, 766

Cohen, M., Harvey, P. M., Schwartz, R. D., & Wilking, B. A. 1984, *ApJ*, 278, 671

Cohen, M., & Schwartz, R. D. 1987, *ApJ*, 316, 311

Cushing, M. C., Vacca, W. D., & Rayner, J. T. 2003, *PASP*, submitted

Davis, C. J., Ray, T. P., Eisloffel, J., & Corcoran, D. 1997, *A&A*, 324, 263

Davis, C. J., Stern, L., Ray, T. P., & Chrysostomou, A. 2002, *A&A*, 382, 1021

Davis, J. E. 2001, *ApJ*, 562, 575

Dempsey, R. C., Linsky, J. L., Fleming, T. A., and & Schmitt, J. H. M. M. 1993, *ApJS*, 86, 599

Drake, S. A., Simon, T., & Linsky, J. L. 1989, *ApJS*, 71, 905

Eisloffel, J., & Mundt, R. 1997, *AJ*, 114, 280

Feigelson, E. D., Broos, P., Gaffney, J. A., III, Garmire, G., Hillenbrand, L. A., Pravdo, S. H., Townsley, L., & Tsuboi, Y. 2002, *ApJ*, 574, 258

Feigelson, E. D., Gaffney, J. A., III, Garmire, G., Hillenbrand, L. A., & Townsley, L. 2003, *ApJ*, 584, 911

Folha, D. F. M., & Emerson, J. P. 2001, *A&A*, 365, 90

Garden, R. P., Russell, A. P. G., & Burton, M. G. 1990, *ApJ*, 354, 232

Garmire, G. P., Bautz, M. W., Ford, P. G., Nousek, J. A., & Ricker, G. R. 2002, Proc. SPIE, 4851, 3

Gehrels, N. 1986, ApJ, 303, 336

Gibb, A. G. 1999, MNRAS, 304, 1

Gibb, A. G., & Heaton, B. D. 1993, A&A, 276, 511

Gibb, A. G., & Little, L. T. 2000, MNRAS, 313, 663

Gibb, A. G., Little, L. T., Heaton, B. D., & Lehtinen, K. K. 1995, MNRAS, 277, 341

Gibb, A. G., & Davis, C. J. 1998, MNRAS, 298, 644

Goodson, A. P., Winglee, R. M., & Böhm, K.-H. 1997, ApJ, 489, 199

Gredel, R. 1994, A&A, 292, 580

———. 1996, A&A, 305, 582

Greene, T. P., & Lada, C. J. 1996, AJ, 112, 2184

Greene, T. P., & Meyer, M. R. 1995, ApJ, 450, 233

Güdel, M. 2002, ARA&A, 40, 217

Hayashi, M. R., Shibata, K., & Matsumoto, R. 1996, ApJ, 468, L37

Herbig, G. H. 1974, *Draft Catalog of Herbig–Haro Objects, Lick Obs. Bull.*, No. 658

Herbig, G. H., & Kuhi, L. V. 1963, ApJ, 137, 398

Hodapp, K.-W., & Deane, J. 1993, ApJS, 88, 119

Hodapp, K.-W., et al. 1996, New Astronomy, 1, 177

Imanishi, K., Koyama, K., & Tsuboi, Y. 2001, ApJ, 557, 747

Imanishi, K., Tsujimoto, M., & Koyama, K. 2002, ApJ, 572, 300

Jones, B. F., Cohen, M., Wehinger, P. A., & Gehren, T. 1987, PASP, 94, 1260

Kenyon, S. J., Whitney, B. A., Gomez, M., & Hartmann, L. 1993, ApJ, 414, 773

Kleinmann, S. G., & Hall, D. N. B. 1986, ApJS, 62, 501

Kraft, R. P., Burrows, D. N., & Nousek, J. A. 1991, ApJ, 374, 344

Lada, E. A., DePoy, D. L., Evans, N. J., II, & Gatley, I. 1991, ApJ, 371, 171

Lis, D. C., Menten, K. M., & Zylka, R. 1999, ApJ, 527, 856

Maddalena, R. J., Morris, M., Moscowitz, J., & Thaddeus, P. 1986, ApJ, 303, 375

Martin, S. C. 1997, ApJ, 478, L33

Martín, E. L., Rebolo, R., Magazzù, A., & Pavlenko, Ya. V. 1994, A&A, 282, 503

Mercer-Smith, J. A., Cameron, A.G. W., & Epstein, R. I. 1984, ApJ, 279, 363

Mewe, R., Kaastra, J. S., & Liedahl, D. A. 1995, HEASARC Legacy, 6, 16

Mitchell, G. F., Johnstone, D., Moriarty-Schieven, G., Fich, M., & Tothill, N. F. H. 2001, *ApJ*, 556, 215

Moneti, A., & Reipurth, B. 1995, *A&A*, 301, 721

Mundt, R., Ray, T. P., & Raga, A. C. 1991, *A&A*, 252, 740

Najita, J., Carr, J. S., & Tokunaga, A. T. 1996, *ApJ*, 456, 292

Najita, J., Carr, J. S., & Mathieu, R. D. 2003, *ApJ*, 589, 931

Neuhäuser, R. 1997, *Science*, 276, 1363

Ozawa, H., Nagase, F., Ueda, Y., Dotani, T., & Ishida, M. 1999, *ApJ*, 523, L81

Phillips, R. R., Gibb, A. G., & Little, L. T. 2001, *MNRAS*, 326, 927

Preibisch, T., Neuhäuser, R., & Stanke, T. 1998, *A&A*, 338, 923

Rayner, J. T., Toomey, D. W., Onaka, P. M., Denault, A. J., Stahlberger, W. E., Vacca, W. D., Cushing, M. C., & Wang, S. 2003, *PASP*, 115, 362

Reipurth, B., Heathcote, S., Yu, K. C., Bally, J., & Rodríguez, L. F. 2000, *ApJ*, 534, 317

Reipurth, B., Rodríguez, L. F., Anglada, G., & Bally, J. 2002, *AJ*, 124, 1045

Reynolds, S. P. 1986, *ApJ*, 304, 713

Scarrott, S. M., Gledhill, T. M., & Warren-Smith, R. F. 1987, *MNRAS*, 227, 1065

Schwartz, R. D., Burton, M. G., & Herrmann, J. 1997, *AJ*, 114, 272

Shu, F., Najita, J., Ostriker, E., Wilken, F., Ruden, S., & Lizano, S. 1994, *ApJ*, 429, 781

Shu, F. H., Shang, H., Glassgold, A. E., & Lee, T. 1997, *Science*, 277, 1475

Smith, R. G., Sellgren, K., & Tokunaga, A. T. 1989, *ApJ*, 344, 413

Smith, R. K., Brickhouse, N. S., Liedahl, D. A., & Raymond, J. C. 2001, *ApJ*, 556, L91

Snell, R. L., & Edwards, S. 1982, *ApJ*, 259, 668

Solf, J. 1987, *A&A*, 184, 322

Stahler, S. W. 1983, *ApJ*, 274, 822

Strom, K. M., Strom, S. E., & Vrba, F. J. 1976, *AJ*, 81, 308

Strom, K. M., Strom, S. E., Carrasco, L., & Vrba, F. J. 1975, *ApJ*, 196, 489

Terquem, C., Eislöffel, J., Papaloizou, J. C. B., & Nelson, R. P. 1999, *ApJ*, 512, L131

Torrelles, J. M., Ho, P. T. P., Rodríguez, L. F., Cantó, J., & Verdes-Montenegro, L. 1989, *ApJ*, 346, 756

Tsujimoto, M., Koyama, K., Tsuboi, Y., Goto, M., & Kobayashi, N. 2002, *ApJ*, 566, 974

Uchida, Y., & Shibata, K. 1984, *PASJ*, 36, 105

Vacca, W. D., Cushing, M. C., & Rayner, J. T. 2003, *PASP*, 115, 389

Verdes-Montenegro, L., & Ho, P. T. P. 1996, *ApJ*, 473, 929

Walter, F. M. 1986, *ApJ*, 306, 573

Ward-Thompson, D., Chini, R., Krügel, E., André, P., & Bontemps, S. 1995, *MNRAS*, 274, 1219

Whittet, D. C. B., Bode, M. F., Longmore, A. J., Adamson, A. J., McFadzean, A. D., Aitken, D. K., & Roche, P. F. 1988, *MNRAS*, 233, 321

Wiramihardja, S. D., Kogure, T., Yoshida, S., Ogura, K., & Nakano, M. 1989, *PASJ*, 41, 155

Zealey, W. J., Williams, P. M., Sandell, G., Taylor, K. N. R., & Ray, T. P. 1992, *A&A*, 262, 570

Fig. 1.— The field of view observed in X rays with *Chandra*. Shown here is the red image from the Digitized Sky Survey of the STScI. The orientation and sky coverage of the ACIS-S detector chips S0–S4 are shown by the overlay. The back-illuminated chips are S1 and S3. The boresight of the observation is near HH 24 on chip S3. Other HH objects in the field are denoted by the diamond symbols. The locations of the X-ray sources are marked by circles, whose diameters are greatly exaggerated here for visibility.

Fig. 2.— Image in the hard X-ray band (2–8 keV) of the area around SSV 63. The locations of the three VLA radio components of Reipurth et al. (2002) are indicated by crosses.

Fig. 3.— X-ray spectrum of SSV 61 observed with the ACIS-S3 detector on *Chandra* is shown in the top panel. A two-temperature thermal model computed with the APEC plasma emission code and folded through the up-dated ACIS detector response is plotted as a histogram curve. Channels in the observed spectrum have been merged to ensure a minimum of 20 counts per bin. The lower panel shows the contributions of the residuals in each bin to the value of χ^2 .

Fig. 4.— QUIRC near-infrared images of HH 24. (*left*) *J*-band, (*middle*) *H*-band, and (*right*) *K*-band. The angular scale, centering, and orientation are identical for all three panels. Following the usual convention, north is up, east is toward the left. Our estimated 5σ photometric limits are 20.9 mag in *J*, 20.1 mag in *H*, and 18.5 mag in *K*.

Fig. 5.— QUIRC near-infrared images of HH 25–26. (*left*) *J*-band, (*middle*) *H*-band, and (*right*) *K*-band. North is up, east is to the left. Photometric limits are as in the previous figure.

Fig. 6.— The near-infrared (0.8–4.1 μm) spectra of six stars in L1630, observed with the SpeX facility instrument on the IRTF.

Fig. 7.— SpeX *K*-band spectra of SSV 60 (top curve) and SSV 61 (bottom curve), identifying the alkali lines and the 2–0 CO bandhead used for spectral classification. Both spectra have been normalized to the continuum and are offset for clarity.

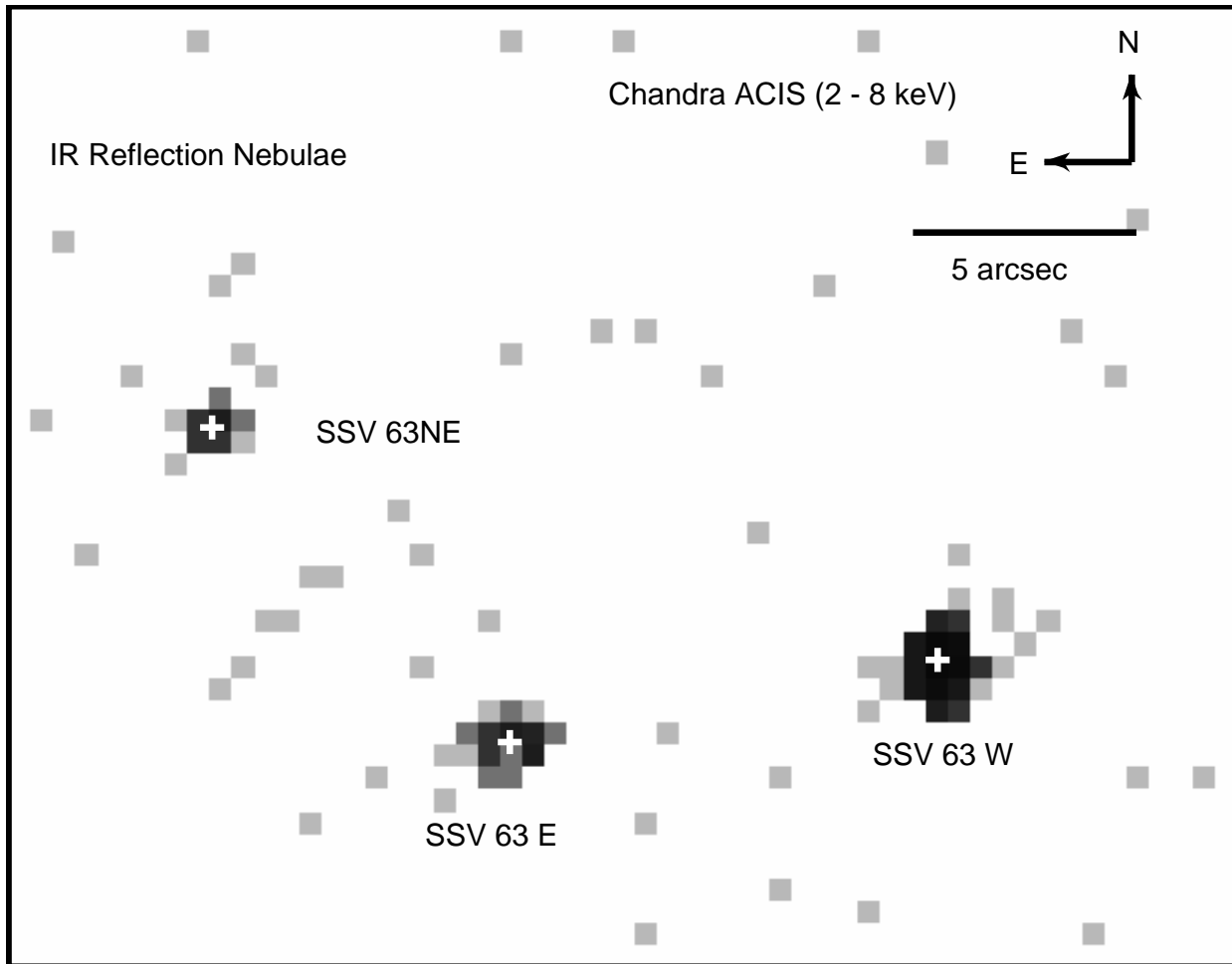
Fig. 8.— SpeX *K*-band spectra of four embedded stars in L1630. They are, in order from top to bottom: SSV 63W (both components combined), SSV 59, SSV 63E, and HH 26-IR. The observed fluxes have been normalized to the continuum and the spectra offset for clarity.

Figure 1 can be obtained from

<http://www.ifa.hawaii.edu/~andrews/figure1.ps>

or with the high-resolution version of this paper at

<http://www.ifa.hawaii.edu/~andrews/L1630.ps>



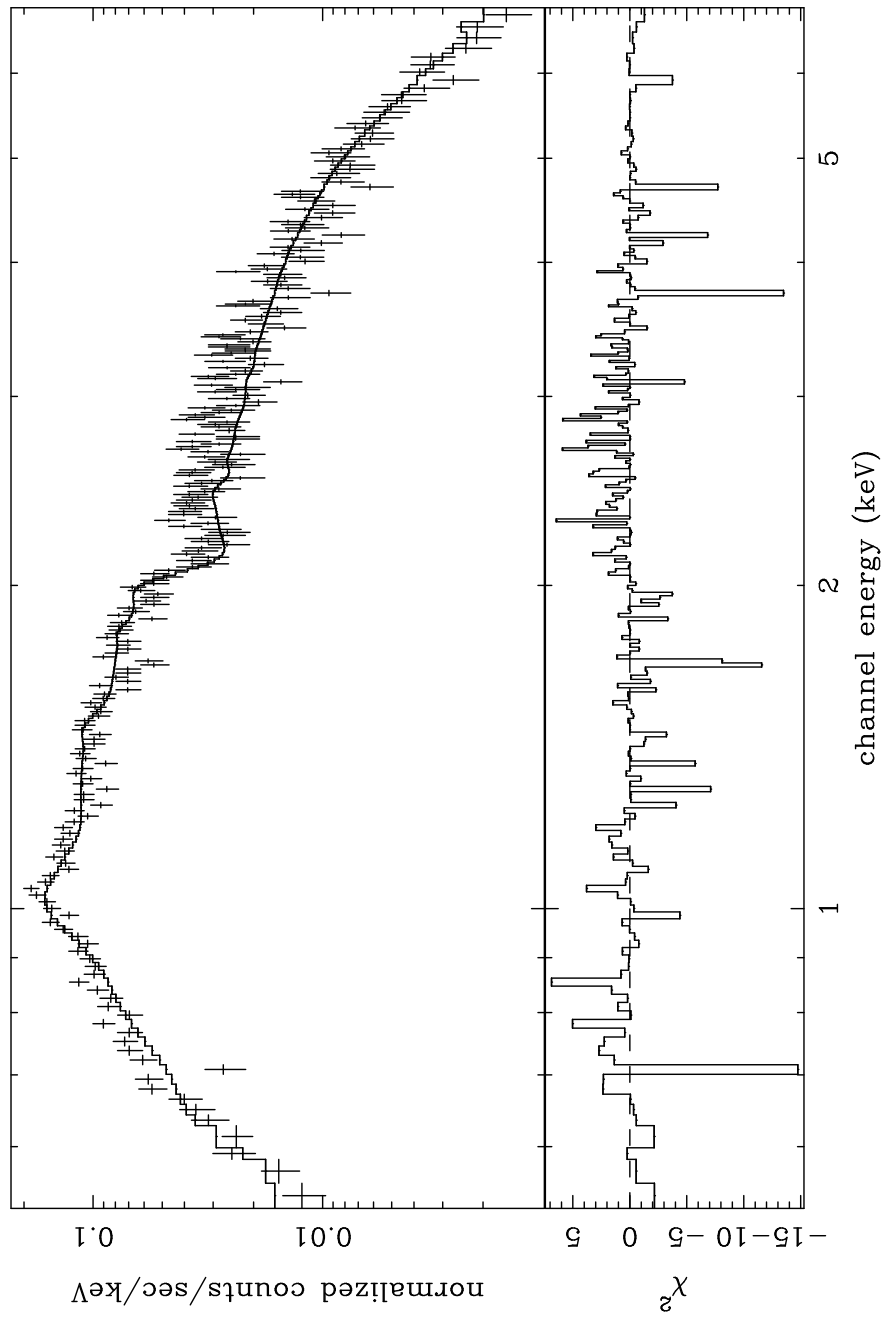


Figure 4 can be obtained from

<http://www.ifa.hawaii.edu/~andrews/figure4.ps>

or with the high-resolution version of this paper at

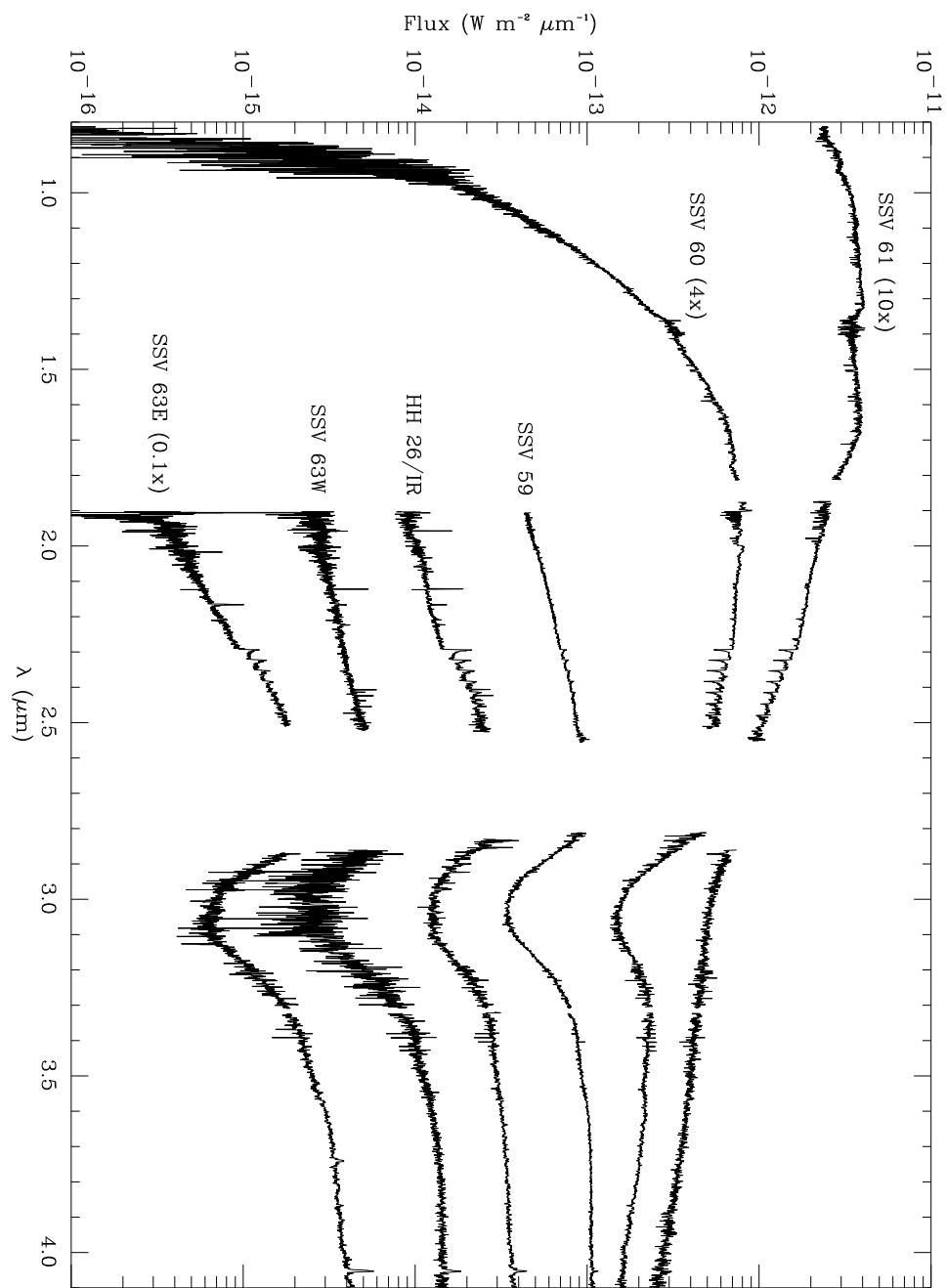
<http://www.ifa.hawaii.edu/~andrews/L1630.ps>

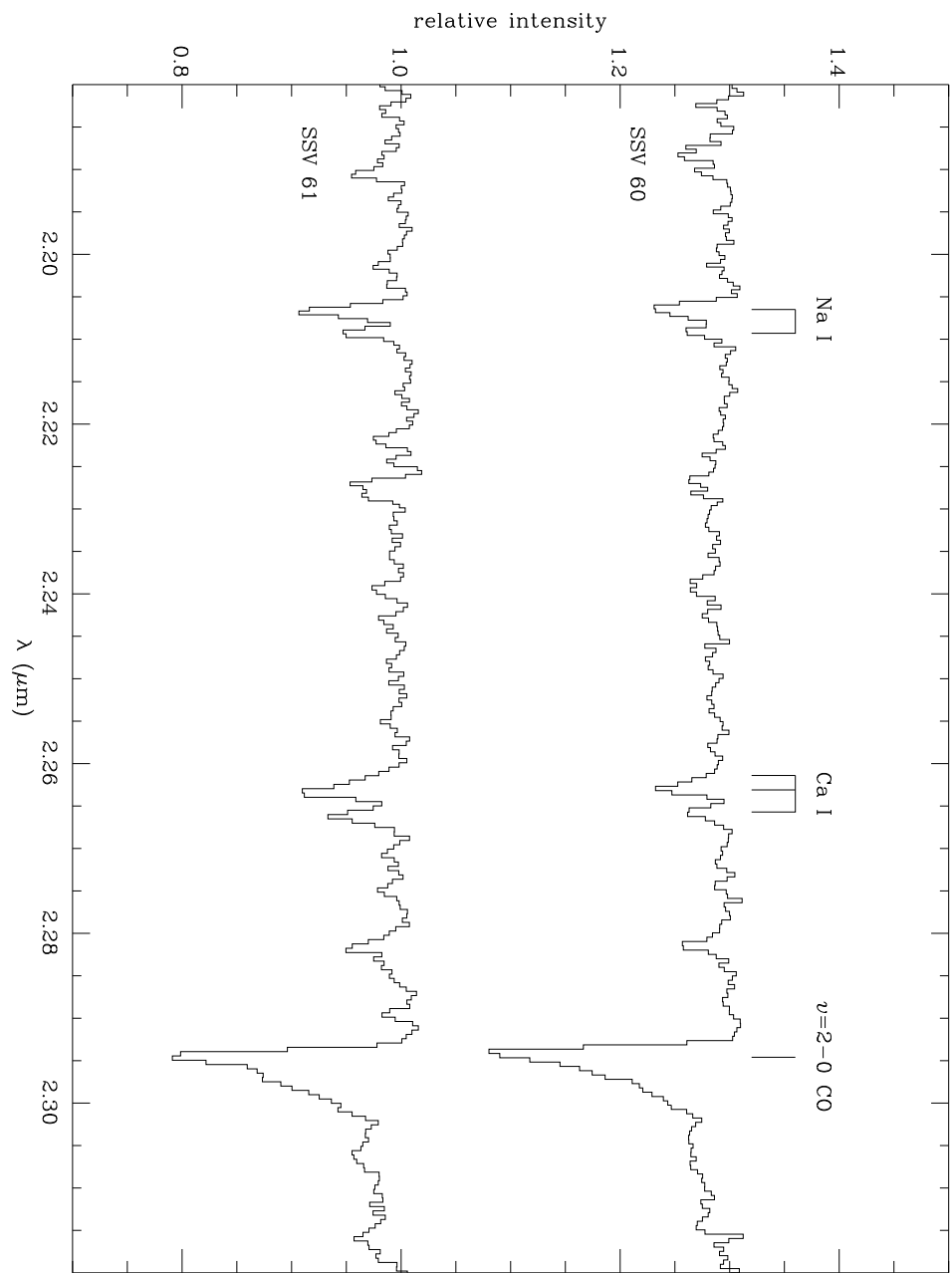
Figure 5 can be obtained from

<http://www.ifa.hawaii.edu/~andrews/figure5.ps>

or with the high-resolution version of this paper at

<http://www.ifa.hawaii.edu/~andrews/L1630.ps>





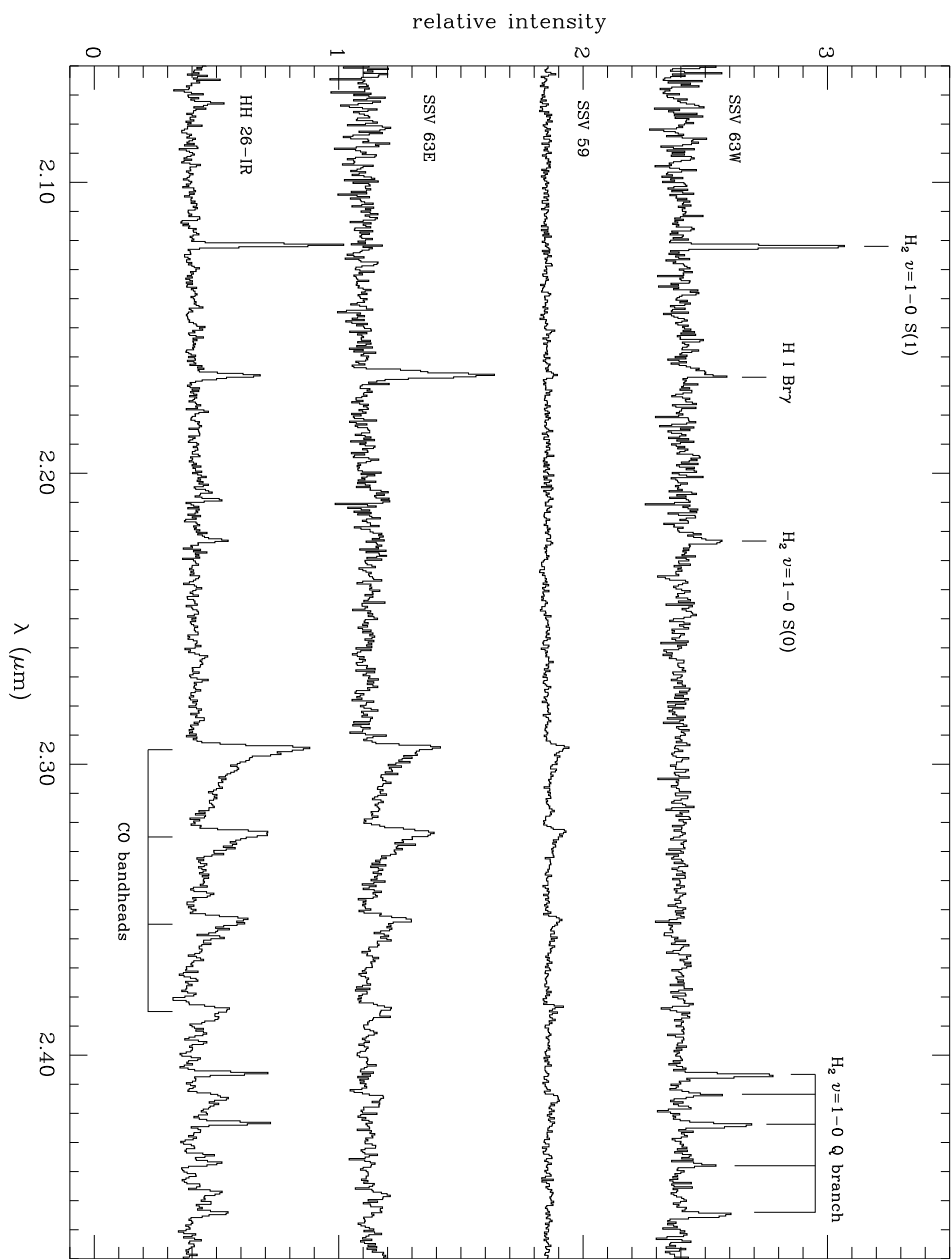


Table 1. X-Ray Detections in L1630

Source	R.A. ^a (J2000)	Decl. ^a (J2000)	θ^b ($'$)	Source Identification	Counts ^c	Count Rate ^d (counts ks^{-1})
1.....	05 45 46.3	-00 15 15	8.5	...	143 ± 15	2.81 ± 0.30
2.....	05 45 51.7	-00 16 33	8.5	...	136 ± 15	2.66 ± 0.30
3.....	05 45 53.1	-00 13 26	6.1	GSC2 S02000123390 (=K α 174)	92 ± 10	1.55 ± 0.17
4.....	05 45 57.8	-00 09 29	3.8	... ^e	94 ± 10	1.54 ± 0.16
5.....	05 46 00.3	-00 08 26	3.5	SSV 65	474 ± 23	8.68 ± 0.42
6.....	05 46 04.2	-00 05 59	4.5	2MASS J05460427-0005591	43 ± 7	0.78 ± 0.13
7.....	05 46 07.8	-00 10 01	1.3	SSV 63W	167 ± 15	2.65 ± 0.24
8.....	05 46 07.8	-00 11 57	2.4	SSV 61	12960 ± 115	251.92 ± 2.23
9.....	05 46 08.1	-00 05 32	4.6	...	20 ± 6	0.36 ± 0.10
10....	05 46 08.5	-00 10 03	1.2	SSV 63E	38 ± 7	0.62 ± 0.11
11....	05 46 08.9	-00 09 56	1.0	SSV 63NE	24 ± 6	0.39 ± 0.10
12....	05 46 09.5	-00 03 31	6.5	2MASS J05460960-0003312	58 ± 8	1.10 ± 0.15
13....	05 46 09.8	-00 05 59	4.0	2MASS J05460984-0005591	29 ± 5	0.52 ± 0.10
14....	05 46 11.6	-00 02 20	7.6	GSC2 S02000125079	498 ± 23	9.69 ± 0.44
15....	05 46 11.6	-00 06 28	3.5	2MASS J05461162-0006279	96 ± 11	1.70 ± 0.19
16....	05 46 12.3	-00 08 08	1.8	2MASS J05461226-0008078	57 ± 8	0.94 ± 0.13
17....	05 46 13.0	-00 18 27	8.5	...	277 ± 18^f	6.76 ± 0.44
18....	05 46 16.3	-00 01 19	8.7	...	68 ± 9	1.34 ± 0.18
19....	05 46 17.7	-00 16 12	6.4	...	67 ± 10^f	1.19 ± 0.18
20....	05 46 18.9	-00 05 38	4.6	GSC2 S020001258	1820 ± 43	32.81 ± 0.78
21....	05 46 19.5	-00 05 20	4.9	SSV 64 (=L α 301)	464 ± 23	9.18 ± 0.45
22....	05 46 20.2	-00 10 20	1.8	2MASS J05462018-0010197	143 ± 14	2.28 ± 0.22
23....	05 46 22.4	-00 08 53	2.6	SSV 68 (=L α 302)	295 ± 18^f	5.45 ± 0.33
24....	05 46 25.9	-00 10 15	3.2	...	47 ± 8	0.79 ± 0.13
25....	05 46 33.3	+00 02 54	13.8	SSV 13	97 ± 14	2.02 ± 0.29

^aUnits of right ascension are hours, minutes, and seconds. Units of declination are degrees, arcminutes, and arcseconds.

^bOff-axis angle measured in arcminutes from the aim point on the ACIS-S3 chip, $\alpha(2000.0) = 05^{\text{h}}46^{\text{m}}13^{\text{s}}1$, $\delta(2000.0) = -00^{\circ}09'57.2'$.

^cBackground-corrected source counts in the 0.5–10 keV energy band. On-source counts were measured through a circular aperture 5'' in radius if $\theta \leq 7'$, and 10'' in radius if $\theta > 7'$. We note that source counts in the narrower 0.5–8.0 keV total band used by some authors, e.g., Feigelson et al. (2002), would be virtually identical to those given here for the wider 0.5–10.0 keV range.

^dCorrected, using a monoenergetic (1.5 keV) exposure map, for the non-uniformity in camera sensitivity across the field of view.

^ePossible non-thermal background radio source, Source no. 1 of Bontemps et al. (1995). See also Anglada et al. (1998).

^fSource located near the edge of a detector chip.

Table 2. X-Ray Fluxes and Luminosities in L1630

Source	Object Class	R.A. ^a (J2000)	Decl. ^a (J2000)	Count Rate ^b (counts ks ⁻¹)	Flux at Earth ^c (10 ⁻¹⁴ ergs cm ⁻² s ⁻¹)	log L_x ^d (ergs s ⁻¹)
SSV 59	I	05 46 04.8	−00 14 17	< 0.20	< 0.40	< 30.03
SSV 60	gK/M	05 46 08.4	−00 14 25	< 0.17	< 0.34	< 29.96
SSV 61	wTTS	05 46 07.8	−00 11 57	251.9 ± 2.2	225 ± 9	31.86
SSV 63W	I	05 46 07.8	−00 10 01	2.65 ± 0.24	5.30 ± 0.52	31.16
SSV 63E	I	05 46 08.5	−00 10 03	0.62 ± 0.11	1.24 ± 0.23	30.52
SSV 63NE	I/0	05 46 08.9	−00 09 56	0.39 ± 0.10	0.78 ± 0.20	30.32
HH 24-MMS ...	0	05 46 08.3	−00 10 43	< 0.17	< 0.34	< 29.96
HH 25-MMS ...	0	05 46 07.3	−00 13 30	< 0.22	< 0.44	< 30.07
HH 26-IR	I	05 46 03.9	−00 14 53	< 0.22	< 0.44	< 30.07
LBS 17-H	0	05 46 30.8	−00 02 40	< 0.12	< 0.24	< 29.81

^aUnits of right ascension are hours, minutes, and seconds. Units of declination are degrees, arcminutes, and arcseconds.

^bBackground-corrected source count rate, adjusted for non-uniform camera response. Upper limits are for a detection cell of radius $r = 5''$ and are significant at the level of 2σ .

^cFlux in the 0.3–10 keV band. Except for SSV 61, we assume that ECF = 2.00×10^{-11} ergs cm⁻² s⁻¹ per count s⁻¹.

^dAbsorption-corrected X-ray luminosity or 2σ upper limit in the 0.3–10 keV band, assuming a distance of $d = 450$ pc and, for all sources except SSV 61, ECF = 5.40×10^{33} ergs s⁻¹ per count s⁻¹. As noted in the text, SSV 60 may be a normal, highly reddened late-K or early-M giant star located behind L1630 at $d \approx 2$ kpc. In general, the uncertainty in L_x for each source is dominated by the uncertainty in the distance of 15% or more.